Polymorphism in Atomically Precise Cu_{23} Nanocluster Incorporating Tetrahedral $[Cu_4]^0$ Kernel

Bao-Liang Han,[†] Zhen Liu,[‡] Lei Feng,[†] Zhi Wang,[†] Rakesh Kumar Gupta,[†] Christine M. Aikens,[*,‡] Chen-Ho Tung,[†] and Di Sun[*,†,§]

[†]Key Laboratory of Colloid and Interface Chemistry, Ministry of Education, School of Chemistry and Chemical Engineering, State Key Laboratory of Crystal Materials, Shandong University, Jinan, 250100, People's Republic of China.
[‡]Department of Chemistry, Kansas State University, Manhattan, Kansas 66506, USA.
[§]Shandong Provincial Key Laboratory of Chemical Energy Storage and Novel Cell Technology, and School of Chemistry and Chemical Engineering, Liaocheng University, Liaocheng 252000, People's Republic of China.

ABSTRACT: Due to the typical instability of copper nanoclusters, atom-precise structural elucidation of these nanoclusters has remained elusive. Herein, we report an air- and moisture-stable 23-copper nanocluster (**SD/Cu23a** or **SD/Cu23b**) isolated from the reaction of $Cu(CF_3COO)_2$, $^tBuC{\equiv}CH$, Cu powder and Ph_2SiH_2 using a gradient reduction ($Cu^{II}{\rightarrow}Cu^{I}{\rightarrow}Cu^0$) strategy (GRS) which is competent to control the kinetics of the reduction reaction, thus avoiding formation of pure Cu^I complexes or large Cu^0 nanoparticles. The solid-state structure of the Cu_{23} nanocluster shows a rare $[Cu_4]^0$ tetrahedral kernel surrounded by an outer Cu_{19} shell which is protected by $^tBuC{\equiv}C^-$ and CF_3COO^- ligands. The Cu_{23} nanocluster is a rare four-electron superatom with a $1S^21P^2$ electronic shell closure and can be crystallized in two polymorphs (*R*3c and *R*-3) depending on the solvent used. The crystallization of **SD/Cu23a** in the *R*-3c space group is mainly governed by van der Waals forces and C-H···F interactions, whereas additional intermolecular C-H···$Cl_{chloroform}$ interactions are responsible for the *R*-3 space group of **SD/Cu23b**. This work not only shows the ingenuity of a gradient reduction strategy for the synthesis of copper nanoclusters but also provides a better fundamental understanding of how to produce the polymorphic copper nanoclusters in a precisely tunable fashion.

INTRODUCTION

Atomically precise group 11 (i.e., Cu, Ag and Au) metal nanoclusters, a key bridge between molecular complexes and plasmonic nanoparticles, have been comprehensively studied in the past decades owing to their aesthetically beautiful molecular structures and fascinating properties such as quantized electronic absorption, fluorescence, and catalysis, to name but a few general examples.[1] Since the breakthroughs in the study of metal nanoclusters such as Au_{102}(*p*-MBA)$_{44}$ and Ag_{44}(*p*-MBA)$_{30}^{4-}$ revealed by single-crystal X-ray diffraction (SCXRD),[2] the number of gold, silver and alloyed nanoclusters with fully determined structures has been upsurging.[3] Based on their structural information, we also have gained deep understanding into their metallic kernel structure, the interfacial bonding between metal and ligand, the spatial arrangement of capping ligands, the growth/evolution mechanisms and even the correlation between properties and structures,[4] all of which are difficult to access for metal nanoparticles mainly characterized by transmission (TEM) and scanning (SEM) electron microscopes.

In contrast to gold and silver, as their lighter congeners, copper nanoclusters remain one of the most daunting challenges facing synthetic chemists, which is consistent with the fact that there are very few Cu^0 coordination complexes available to date.[5] Although the Liu group has isolated a family of Cu^I hydride clusters protected by dithiophosphates such as $[Cu_{20}H_{11}\{S_2P(O^iPr)_2\}_{29}]$,[6] $[Cu_{28}H_{15}(S_2CNR)_{12}]PF_6$,[7] and $[Cu_{32}H_{20}\{S_2P(O^iPr)_2\}_{12}]$[8] using diverse reductants, they still lack any Cu^0 character. The main reasons responsible for scarcity of Cu^0 nanocluster are i) lower susceptibility to reduction of Cu^I precursors and ii) higher susceptibility to oxidation of as-formed products, which render the isolation of air- and moisture-stable products more challenging. Until recently, few nanoclusters with zero-valent copper characteristics were successfully synthesized including $[(Cp^*AlCu)_6H_4]$,[9] $[Cu_{25}H_{22}(PPh_3)_{12}]Cl$,[10] $[Cu_{29}Cl_4H_{22}(L1)_{12}]Cl$ (L1 = 4,7-diphenyl-1,10-phenanthroline),[11] $[Cu_{43}(AlCp^*)_{12}]$,[12] $[Cu_{13}\{S_2CN^nBu_2\}_6(C{\equiv}CC(O)OMe)_4]^+$,[13] and $[Cu_{53}(CF_3COO)_{10}(^tBuC{\equiv}C)_{20}Cl_2H_{18}]^+$.[14] However, most of them contain interstitial H^- ions, which may make the arrangement of Cu atoms in the cluster very different from those packed in actual copper nanoparticles or even metallic copper. Thus, exploring suitable protection ligands, reductants, and reaction strategy for the synthesis of Cu^0 nanoclusters containing as few H^- atoms as possible would be highly desirable, although these experiments are quite challenging.

On the basis of the above considerations, we envisaged a gradient reduction strategy (GRS) to realize the valence of Cu atom evolving from +2 to +1 then to 0 by using different reductants at different stages. Inspired by the comproportionation of Cu powder and Cu^{II} salt to produce Cu^I species,[15] we further promoted the reduction reaction forward one step to get Cu^0-containing nanoclusters, $[Cu_{23}(^tBuC{\equiv}C)_{13}(CF_3COO)_6]$ (**SD/Cu23a**) or $[Cu_{23}(^tBuC{\equiv}C)_{13}(CF_3COO)_6]{\cdot}CHCl_3$ (**SD/Cu23b**), which not only shows solvent-dependent polymorphism but also exemplifies the effectiveness of GRS. The Cu_{23} nanocluster shows the following characteristics: i) it contains a scarce $[Cu_4]^0$ tetrahedral kernel surrounded by an outer Cu_{19} shell; ii) it is a rare four-electron superatom with $1S^21P^2$ electronic shell closure; and iii) it can be crystallized in two polymorphs (*R*3c and *R*-3) depending on the solvent used, which helps us to recognize the dominant forces in forming different cluster packing fashions in crystals.

Scheme 1. Synthetic Route for **SD/Cu23a** and **SD/Cu23b**.

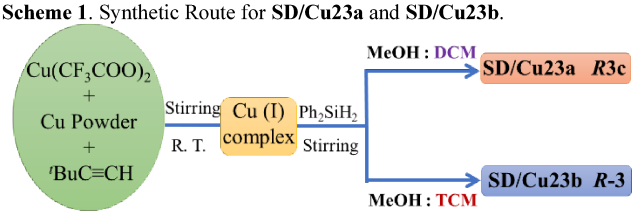

RESULTS AND DISCUSSION

Synthesis Discussion

The overall synthesis of the Cu_{23} nanocluster involves two steps where two different reductants were utilized in respective steps (Scheme 1). Briefly, **SD/Cu23a** was prepared by the reaction of $Cu(CF_3COO)_2$ and $^tBuC{\equiv}CH$ in CH_2Cl_2/CH_3OH in the presence of Cu powder as reductant at room temperature. This is the first step of the reaction that makes the initial blue solution change to yellow-green, indicating that Cu^I species were formed as observed in the previous Cu^I cluster systems.[16] Addition of Ph_2SiH_2 to the foregoing solution made the color change from yellow-green to orange, suggesting the formation of Cu^0 species. The stepwise color evolution indicates the usefulness of GRS (Figure S1a). The gradual reduction of Cu^{II} to Cu^I then to Cu^0 using two reagents of different reducing ability can avoid the formation of i) large Cu^0 nanoparticles due to fast reduction kinetics if using a strong reducing reagent such as $NaBH_4$, or ii) pure Cu^I nanoclusters due to the insufficient reduction ability of Ph_2SiH_2. The reducing abilities of Cu powder and Ph_2SiH_2 may match well with the redox potentials of Cu^{II}/Cu^I and Cu^I/Cu^0 in the current reaction medium, respectively. The orange block crystals of **SD/Cu23a** can be crystallized after five days and collected together by filtration as bulk samples (~20% yield). The crystalline sample of **SD/Cu23a** can maintain its color and morphology unchanged for at least two months at ambient environment, which demonstrates its stability to light, moisture and oxygen in solid state, as supported by UV-Vis spectra before and after aging (Figure S1b). If we added two reductants into the mixture of $Cu(CF_3COO)_2$ and $^tBuC{\equiv}CH$ together, the initial blue solution does not change to orange, even elongating the stirring time to 24h. If only Ph_2SiH_2 was used, the resulting mixture is a light yellow solution from which nothing can be crystallized. If the above synthesis is performed in $CHCl_3/CH_3OH$, we can isolate **SD/Cu23b** as red rod crystals with a yield of 5%. **SD/Cu23a** and **SD/Cu23b** crystallized into different space groups, in spite of possessing the same trigonal crystal system. The use of $Cu(CF_3COO)_2$ in the synthesis of **SD/Cu23a** or **SD/Cu23b** is very important because we cannot isolate any crystalline products if we utilize $Cu(NO_3)_2$, $Cu(OAc)_2$ or $CuSO_4$. The synthesis details of **SD/Cu23a** and **SD/Cu23b** are shown in the Supporting Information (SI). **SD/Cu23a** was collected and characterized by a suite of standard chemical characterization methods, including powder X-ray diffraction (PXRD), IR, elemental analysis, and energy dispersive X-ray spectrometry (EDS) elemental mapping (Figure S5-S7). Density functional theory (DFT) calculations were also performed on **SD/Cu23a** for understanding the electronic structure and optical properties in detail. Electrospray ionization mass spectrometry (ESI-MS) of **SD/Cu23a** dissolved in $CHCl_3$ did not provide useful information even adding CsOAc to help ionization, which suggests i) **SD/Cu23a** is neutral and is hard to ionize under mass spectrometer conditions, or ii) it is fragmented in the ionization process.[17]

X-Ray Structures of SD/Cu23a and SD/Cu23b

SCXRD revealed that **SD/Cu23a** and **SD/Cu23b** crystallize in a trigonal unit cell under the *R*3c and *R*-3 space groups, respectively. Due to the similarity of these two nanoclusters, we only present the atomic structure of **SD/Cu23a**. The difference of the cluster packing in the unit cell will be discussed at the end of this section. Based on the crystallographic structure analysis, the cluster is trisected based on the C_3 principle axis, giving only one-third of the cluster in the asymmetric unit and the composition of **SD/Cu23a** is $[Cu_{23}(^tBuC{\equiv}C)_{13}(CF_3COO)_6]$ (Figure 1a and 1b). No counterions and solvents were observed and no guests occupying voids in the unit cell were detected using PLATON,[18] which indicates that the Cu_{23} nanocluster is neutral. Based on its formula, only 19 anionic ligands (13 $^tBuC{\equiv}C^-$ and 6 CF_3COO^-) are found, with no additional anions in the unit cell; these 19 anionic ligands would not balance the charge if all 23 Cu atoms are in the +1 oxidation state, so four of the 23 Cu atoms must effectively have a zero valence. Considering the short Cu···Cu distances and narrow distribution of distances in the central Cu_4 tetrahedron which are similar to the highly ordered structure of the bulk metal Cu, we tentatively assigned this central Cu_4 tetrahedron as a neutral kernel. Accordingly, **SD/Cu23a** should be a 4e superatom. Hirshfeld partial charges (Table S1) show that the five core atoms, especially the Cu_4 tetrahedron, are essentially neutral, whereas the Cu atoms in the outer shell are more positively charged. To further verify the mixed valent (Cu^0/Cu^I) nature of **SD/Cu23a**, X-ray-excited Auger electron spectroscopy was performed and clearly shows two different LMM Auger kinetic energies at 918.54 and 915.26 eV (Figure S1c), corresponding to Cu^0 and Cu^I, respectively.[19]

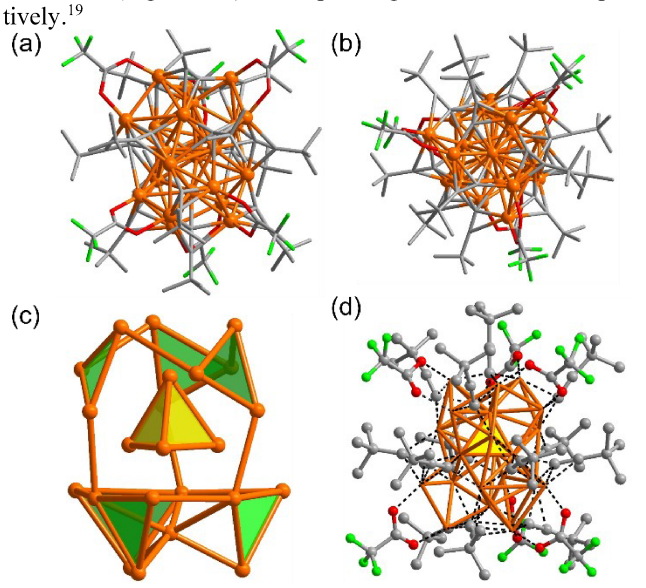

Figure 1. (a) and (b) Total structure of the Cu_{23} nanocluster viewed side and top along the C_3 axis. (c) The metallic framework of the Cu_{23} nanocluster containing a Cu_4 tetrahedron in center. (d) The coordination fashions of ligands (coordination bonds are shown in black dashed lines) and their distributions on the surface of the Cu_{23} nanocluster. Color labels: Orange, Cu; green, F; gray, C; red, O.

SD/Cu23a contains a metallic framework of 23 copper atoms (Figure S2a) which, at first glance, resembles a severely distorted icosahedron with Cu4 as a center (Figure S2b) face-fusing with another severely distorted cuboctahedron with Cu5 as the center (Figure S2c). The Cu4 and Cu5 coordinate to the twelve vertexes of the icosahedron and the nine vertexes of the cuboctahedron with Cu···Cu separations of 2.57-3.07 Å and 2.44-3.04 Å, respectively. This Cu_{23} core is similar to the Au_{23} core in the Au_{38} cluster[20] but is severely distorted from an ideal bi-icosahedron.

Alternatively, we deemed this metallic framework as a Cu_4 tetrahedron surrounded by an outer Cu_{19} shell (Figure 1c). The vertex (Cu4) of the Cu_4 tetrahedron has a coordination number of 12, slightly lower than that in metallic Cu.[21] The Cu···Cu distances within the Cu_4 tetrahedron fall in the range of 2.60-2.68 Å with an average value of 2.64 Å, which is a little bit longer than those in Cu metal (2.556 Å),[22] but still comparable to those in Cu^0-containing clusters.[10] Of note, Cu5 triply coordinates to the base of Cu_4 tetrahedron with Cu···Cu distances beyond 3 Å, ruling out the possible trigonal bipyramidal core of five Cu atoms. The Cu···Cu distances in the Cu_{19} shell span in a wider range of 2.44-2.89 Å. Although the pure metal tetrahedral kernel has been widely observed in Au nanoclusters and was seen as an important subunit in the "Au_4 tetrahedron-based vertex-sharing" growth mode,[22] the isolated Cu_4 tetrahedral kernel has been rarely observed and the only example is a Cu_{20} nanocluster carrying a $[Cu_4]^{2+}$ tetrahedral kernel inside.[23] The structural elucidation of such an ultra-small Cu kernel will help us to understand the cluster growth from small subunits into a larger, overall structure. As homonuclearity counterparts, two Au_{23} nanoclusters ($[Au_{23}(SR)_{16}]$ and $[Au_{23}(PhC{\equiv}C)_9(Ph_3P)_6]$) have been reported by the Jin and Wang groups, respectively.[24] The $[Au_{23}(SR)_{16}]$ shows a bipyramidal Au_{15} kernel and trimeric $Au_3(SR)_4$ motif, whereas $[Au_{23}(PhC{\equiv}C)_9(Ph_3P)_6]$ is comprised of a D_{3h} Au_{17} kernel surrounded by three PhC≡C-Au-PhC≡C-Au-PhC≡C motifs. Both of them have completely different arrangements of metal atoms in the kernel compared to those in **SD/Cu23a**.

On the surface of the Cu_{23} framework, 13 ^{t}BuC≡C$^-$ ligands are distributed into four layers along the C_3 axis, containing 1, 3, 6, and 3 ^{t}BuC≡C$^-$ ligands (Figure S3). One of two poles is occupied by one μ_4-η^1:η^1:η^1:η^1 ^{t}BuC≡C$^-$ ligand. There are three μ_3-η^1:η^1:η^1 and three μ_4-η^2:η^1:η^1:η^1 ligands ligated in the equatorial region. Between the two poles and the equator, there are two mixed-ligand layers each consisting of three alternating ^{t}BuC≡C$^-$ and CF_3COO^- (κ_2-η^1:η^1) ligands. Interestingly, these six ^{t}BuC≡C$^-$ ligands take different coordination modes (3 in μ_4-η^2:η^2:η^1:η^1 and 3 in μ_3-η^1:η^1:η^1) in different layers (Figure 1d). The Cu-C and Cu-O distances are in the ranges of 1.92-2.42 and 1.93-2.03 Å, respectively.

The structure of **SD/Cu23b** is quite similar to that of **SD/Cu23a**, but it crystallized as a $CHCl_3$ solvate which dramatically changed the cluster packing in the unit cell, thus giving a different space group with respect to **SD/Cu23a**. Both clusters have two poles that lie along a crystallographic 3-fold axis with only one pole occupied by a σ-bonded ^{t}BuC≡C$^-$ ligand. Thus if looking at this C_3 axis, we can define the "head" and "tail" as the poles with and without the ^{t}BuC≡C$^-$ ligand, respectively. Interestingly, as shown in Figure 2a and 2c, **SD/Cu23a** exhibits a head-to-tail packing along the *c* axis through van der Waals forces and C-H···F interactions, whereas a displaced head-to-head packing fashion was observed in **SD/Cu23b** viewed along the same direction. Such a unique packing mode in **SD/Cu23b** forms a double layer structure running along the *ab* plane through similar supramolecular interactions. The double layer as a unit is further separated by a layer of $CHCl_3$. Each $CHCl_3$ is intercalated into a void formed by four **SD/Cu23b** arranged in a tetrahedron through the C-H···Cl interactions that are not available in **SD/Cu23a**. (Figure S4). The simplified cluster packing patterns of **SD/Cu23a** and **SD/Cu23b** are shown in Figure 2b and 2d, respectively. The formation of polymorphic Cu_{23} nanoclusters may be mainly dictated by the C-H···Cl interactions. $CHCl_3$ has one more Cl atom than CH_2Cl_2, which increases the chance for the formation of C-H···Cl interactions during cluster crystallization.

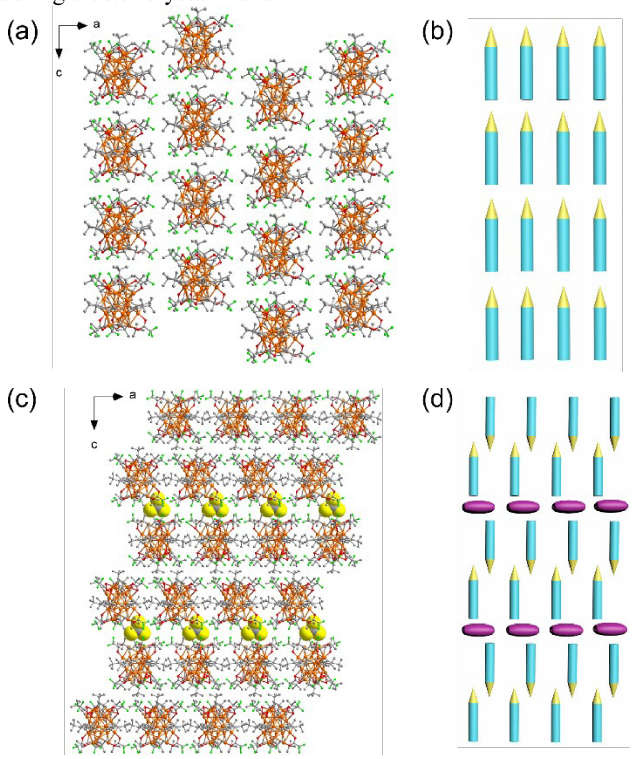

Figure 2. The head-to-tail (a) and head-to-head (c) cluster packing fashions found in **SD/Cu23a** and **SD/Cu23b**. Color labels: Orange, Cu; green, F; yellow, Cl; gray, C; red, O. Simplified cluster packing in **SD/Cu23a** (b) and **SD/Cu23b** (d). Object labels: Pointed cylinder, Cu_{23} nanocluster; purple ellipse, $CHCl_3$.

Density Functional Theory (DFT) Calculations and Electronic Structure

SD/Cu23a can be dissolved well in CH_2Cl_2 or $CHCl_3$ to give a pale yellow solution which can change to green within one hour if exposed to air at ambient environment, indicating **SD/Cu23a** cannot maintain long-term stability in solution likely due to the oxidation of Cu(I) to Cu(II) by O_2 in air. Thus, the UV-Vis spectrum of **SD/Cu23a** in $CHCl_3$ was measured in a tightly capped cuvette and showed an unstructured profile with an absorption onset at 550 nm, which is quite similar to the theoretical absorption spectrum (Figure 3). Compared to the unstructured UV-Vis profile of **SD/Cu23a**, $[Au_{23}(SR)_{16}]$ and $[Au_{23}(PhC{\equiv}C)_9(Ph_3P)_6]$) exhibit distinct peaks in the visible region at 570 and 524 nm, respectively.[24]

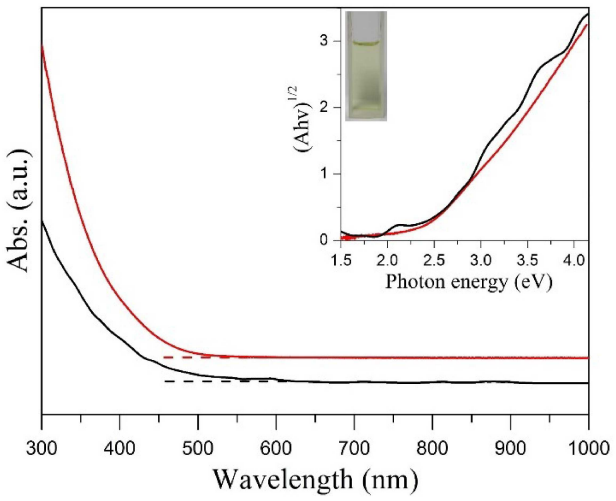

Figure 3. The experimental UV-Vis absorption (red line) in comparison with the calculated spectrum (black line) of **SD/Cu23a**. Inset: Experimental (red line) and the calculated (black line) photon-energy plots of **SD/Cu23a**.

Based on the DFT calculations, the shape of the absorption spectrum of **SD/Cu23a** primarily comes from its high density of states (DOS) without any strong dominating transitions. As shown in Table S2, the first ten excitations in $[Cu_{23}(^tBuC{\equiv}C)_{13}(CF_3COO)_6]$ lie in the energy range between 0.4 to 1.2 eV and arise from transitions from the HOMO to LUMO through LUMO+9. The weak oscillator strength for these excitations yields an absorption spectrum with a relatively flat absorption intensity from 0 to 2 eV. The first excitation at 0.43 eV mostly comes from the HOMO-LUMO transition with a weight of 0.9884 and is essentially an sp←sp intraband transition. This small excitation energy is reasonable due to the relatively small HOMO-LUMO gap (0.398 eV) in the Kohn-Sham orbital levels. Except for the 8th and 9th excitations, the weights of the transitions primarily responsible for the first ten excitations are above 0.9, which indicate that these correspond to single-particle transitions from the HOMO to the LUMOs. These transitions are not observed in the experimental UV-Vis spectrum, which is likely due to their low oscillator strengths. The theoretical UV-vis spectrum is more defined than the experimental spectrum, which may be due to the vibrational broadening at room temperature, cluster-solvent interactions, or other factors.

As shown in Table S3, Figure 3, and Figure S13 the highest oscillator strengths for any excited state in the UV-Vis region are all small (less than 0.1). In consequence, no single distinctive transition dominates the absorption spectrum. The high intensity is a result of a high density of states. The excitation around 3.18 eV has a relatively high oscillator strength value (0.0905) due to the inclusion of three transitions with similar weight (HOMO-25 → LUMO+3, HOMO-17 → LUMO+6, HOMO-26 → LUMO+3). The HOMO-17, HOMO-25, and HOMO-26 are mixture of 3d atomic orbitals from copper mixed with carbon 2p orbitals.

The frontier Kohn-Sham orbitals of the **SD/Cu23a** cluster are shown in Figure 4. The HOMO has a P-like character that mostly come from the 4sp and 3d atomic orbitals of copper atoms in the core; the P-like character arises because of the nodal plane in the HOMO orbital. Distorted π bonds between carbon atoms also contribute to this HOMO. The appearance of this orbital provides support for the assignment of this nanoparticle as a 4e ($1S^21P^2$) superatom.[25] The 1S orbital lies significantly lower in energy than the HOMO, ligand-based orbitals, and the copper 3d band.

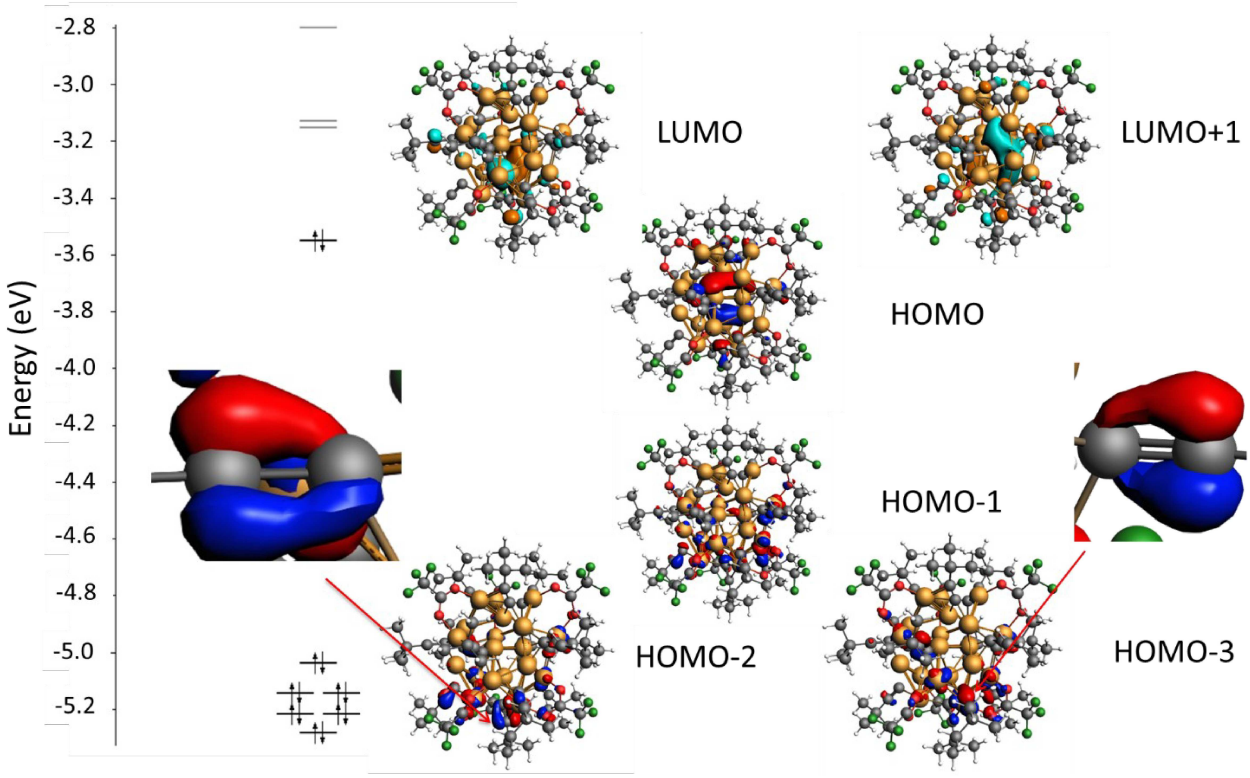

Figure 4. Kohn-Sham orbitals and orbital energy diagram for **SD/Cu23a**. Insets in the figure display representative alkyne (C≡C) bonds. Color labels: Orange, Cu; green, F; gray, C; red, O.

In the HOMO-1, the orbital has significant contribution from π orbitals from carbon-carbon triple bonds. The orbital energy diagram also features a relatively large energy gap (1.486 eV) between the HOMO and HOMO-1 and a relatively small gap (0.398 eV) between HOMO-LUMO. The calculation suggests that $[Cu_{23}(CF_3COO)_6(^tBuC{\equiv}C)_{13}]^{2+}$ would possibly be a stable charge state for this nanoparticle under other experimental conditions (e.g. in polar solvents in the presence of counterions).

HOMO-2 is another orbital with π-like character between carbon-carbon triple bonds, where the lobes of the π orbitals are larger towards the tertbutyl groups. Like HOMO-2, the character of HOMO-3 also shows significant contribution from carbon-carbon triple bonds. Contributions from carboxylate groups increase in this orbital. The similarity of the HOMO-2 and HOMO-3 molecular orbitals can also be seen in the degeneracy in their Kohn-Sham energy levels. Orbitals directly below the HOMO-3 have significant contributions from carbon π orbitals, with the copper 3d band below.

For **SD/Cu23a**, the LUMO primarily arises from copper atoms in the core of cluster. Both LUMO and LUMO+1 have approximate 1P character. The LUMOs immediately above the LUMO+1 primarily come from π* orbitals from carbon-carbon bonds, although some orbitals also have large contributions from the Cu 4sp orbitals.

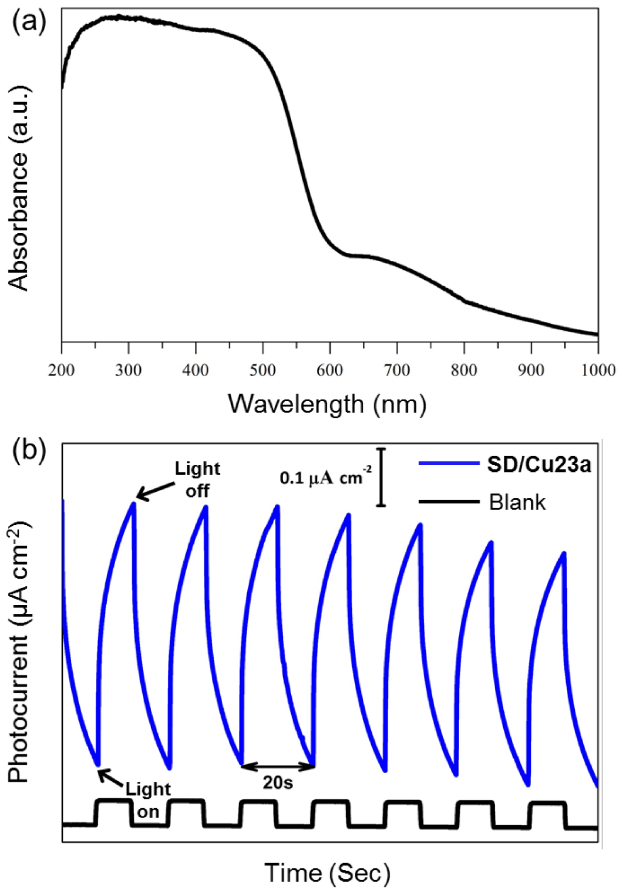

Figure 5. (a) The solid-state UV-Vis spectrum of **SD/Cu23a**. (b) Comparison of photocurrent responses of blank and **SD/Cu23a** ITO electrodes in a 0.2 M Na_2SO_4 aqueous solution under repetitive irradiation.

UV-Vis Spectrum and Photocurrent Response Properties of SD/Cu23a

The solid-state UV-Vis absorption spectrum of **SD/Cu23a** was recorded using the diffuse reflectance mode at room temperature in the wavelength range from 200 to 1000 nm. As depicted in Figure 5a, there is a wide absorption band covering the UV and visible regions (250-500 nm). This high energy absorption should originate from a mixture of π→π* transition of $^tBuC{\equiv}C^-$ and ligand-to-metal charge transfer. Based on the Kubelka–Munk function (Figure S8), a characteristic energy gap of **SD/Cu23a** was estimated to be 1.45 eV. Based on the DFT calculations, this may correspond to the 1.486 eV gap between the core-based HOMO orbital and the ligand-based orbitals (HOMO-1 and below). The sharp increase in absorbance centered around 1.8 eV in Figure S8 is likely due to the start of ligand-to-metal excitations arising out of the ligand-based orbitals which are predicted to begin around 1.9 eV based on the DFT calculations. Of note, **SD/Cu23a** is non-emissive in solution and solid state, even at liquid nitrogen temperature.

Considering the broad absorption in the UV-Vis region, the photoelectrochemical properties of **SD/Cu23a** was tested in a typical three-electrode system using ITO glass as the working electrode, platinum wire as the assisting electrode, Ag/AgCl as the reference electrode and keeping the bias voltage at 0.6 V. Generally, the sample is suspended in an ethanol solution, followed by the addition of 10 μL of a dilute solution of naphthol in ethanol (0.5 wt. %), and then spin-coated onto an ITO glass electrode. Upon on−off cycling irradiation with LED light (λ = 420 nm; 50 W; intervals of 10 s), clear photocurrent responses were observed compared to the blank ITO glass (Figure 5b) and showed a gradual increase or decrease of the photocurrent density in the presence or absence of light irradiation which indicates that **SD/Cu23a** has a good generation and separation efficiency of photoinduced electrons/holes pairs in ITO electrodes but the electron transport is not very good, thus producing delayed generation or decay of photocurrent responding to turning the light irradiation on or off.

CONCLUSIONS

In summary, we employed a gradient reduction strategy involving reduction of Cu^{II} to Cu^0 through Cu^I to synthesize an air- and moisture-stable 23-copper nanocluster which can crystallize into two polymorphs (*R*3c and *R*-3) controlled by the solvents. The Cu_{23} cluster contains a rare $[Cu_4]^0$ tetrahedral kernel surrounded by an outer Cu_{19} shell, giving a typical core-shell structure. The cluster packing in the solid state was governed by solvent to give head-to-tail and head-to-head double layer structures for **SD/Cu23a** and **SD/Cu23b**, respectively. This work not only developed an effective gradient reduction strategy for the synthesis of copper nanocluster but also provides a better fundamental understanding of how the solvent influences the packing of copper nanoclusters to produce the polymorphs.

ASSOCIATED CONTENT

Supporting Information. Experimental and computational details, detailed crystallographic structure and data including the CIF file,

PXRD and IR. This information is available free of charge via the internet at http://pubs.acs.org.

AUTHOR INFORMATION

Corresponding Author

dsun@sdu.edu.cn (D. S.)
cmaikens@ksu.edu (C. A.)

ORCID

Di Sun: 0000-0001-5966-1207

Christine Aikens: 0000-0002-0854-7997

Notes

The authors declare no competing financial interest.

ACKNOWLEDGMENT

This work was financially supported by the National Natural Science Foundation of China (Grant Nos. 91961105, 21822107, 21571115, 21827801), the Natural Science Foundation of Shandong Province (Nos. ZR2019ZD45, JQ201803 and ZR2017MB061), the Taishan Scholar Project of Shandong Province of China (Nos. tsqn201812003 and ts20190908), the Qilu Youth Scholar Funding of Shandong University. Z.L. and C.M.A were supported by the National Science Foundation (CHE-1905048) of the United States. The computing for this work was performed on the Beocat Research Cluster at Kansas State University, which is funded in part by NSF grants CHE-1726332, CNS-1006860, EPS-1006860, and EPS-0919443.

REFERENCES

1) (a) Aikens, C. M. Electronic and Geometric Structure, Optical Properties, and Excited State Behavior in Atomically Precise Thiolate-Stabilized Noble Metal Nanoclusters. *Acc. Chem. Res.* **2018**, *51*, 3065-3073; (b) Bhattarai, B.; Zaker, Y.; Atnagulov, A.; Yoon, B.; Landman, U.; Bigioni, T. P. Chemistry and Structure of Silver Molecular Nanoparticles. *Acc. Chem. Res.* **2018**, *51*, 3104-3113; (c) Gan, Z.; Xia, N.; Wu, Z. Z. Discovery, Mechanism, and Application of Antigalvanic Reaction. *Acc. Chem. Res.* **2018**, *51*, 2774-2783; (d) Ghosh, A.; Mohammed, O. F.; Baker, O. M. Atomic-Level Doping of Metal Clusters. *Acc. Chem. Res.* **2018**, *51*, 3094-3103; (e) Kwak, K.; Lee, D. Electrochemistry of Atomically Precise Metal Nanoclusters. *Acc. Chem. Res.* **2019**, *52*, 12-22; (f) Li, J.; Ma, H. Z.; Reid, G. E.; Edwards, A. J.; Hong, Y.; White, J. M.; Mulder, R. J.; O'Hair, R. A. J. Synthesis and X-Ray Crystallographic Characterisation of Frustum-Shaped Ligated $[Cu_{18}H_{16}(DPPE)_6]^{2+}$ and $[Cu_{16}H_{14}(DPPA)_6]^{2+}$ Nanoclusters and Studies on Their H_2 Evolution Reactions. *Chem. - Eur. J.* **2018**, *24*, 2070-2074; (g) Zhang, Q. F.; Chen, X.; Wang, L. S. Toward Solution Syntheses of the Tetrahedral Au_{20} Pyramid and Atomically Precise Gold Nanoclusters with Uncoordinated Sites. *Acc. Chem. Res.* **2018**, *51*, 2159-2168; (h) Sakthivel, N. A.; Dass, A. Aromatic Thiolate-Protected Series of Gold Nanomolecules and a Contrary Structural Trend in Size Evolution. *Acc. Chem. Res.* **2018**, *51*, 1774-1783; (i) Kang, X.; Zhu, M. Tailoring the Photoluminescence of Atomically Precise Nanoclusters. *Chem. Soc. Rev.* **2019**, *48*, 2422-2457; (j) Yao, Q. F.; Chen, T. K.; Yuan, X.; Xie, J. P. Toward Total Synthesis of Thiolate-Protected Metal Nanoclusters. *Acc. Chem. Res.* **2018**, *51*, 1338-1348; (k) Corrigan, J. F.; Fuhr, O.; Fenske, D. Metal Chalcogenide Clusters on the Border between Molecules and Materials. *Adv. Mater.* **2009**, *21*, 1867-1871; (l) Shichibu, Y.; Zhang, M.; Kamei, Y.; Konishi, K. $[Au_7]^{3+}$: A Missing Link in the Four-Electron Gold Cluster Family. *J. Am. Chem. Soc.* **2014**, *136*, 12892-12895; (m) Kurashige, W.; Niihori, Y.; Sharma, S.; Negishi, Y. Precise synthesis, functionalization and application of thiolate-protected gold clusters. *Coord. Chem. Rev.* **2016**, *320*, 238-250; (n) Kenzler, S.; Schrenk, C.; Schnepf, A. $Au_{108}S_{24}(PPh_3)_{16}$: A Highly Symmetric Nanoscale Gold Cluster Confirms the General Concept of Metalloid Clusters. *Angew. Chem., Int. Ed.* **2017**, *56*, 393-396; (o) Yonesato, K.; Ito, H.; Itakura, H.; Yokogawa, D.; Kikuchi, T.; Mizuno, N.; Yamaguchi, K.; Suzuki, K. Controlled Assembly Synthesis of Atomically Precise Ultrastable Silver Nanoclusters with Polyoxometalates. *J. Am. Chem. Soc.* **2019**, *141*, 19550-19554.

2) (a) Jadzinsky, P. D.; Calero, G.; Ackerson, C. J.; Bushnell, D. A.; Kornberg, R. D. Structure of a Thiol Monolayer-Protected Gold Nanoparticle at 1.1 Angstrom Resolution. *Science* **2007**, *318*, 430-433; (b) Desireddy, A.; Conn, B. E.; Guo, J.; Yoon, B.; Barnett, R. N.; Monahan, B. M.; Kirschbaum, K.; Griffith, W. P.; Whetten, R. L.; Landman, U.; Bigioni, T. P. Ultrastable Silver Nanoparticles. *Nature* **2013**, *501*, 399-402.

3) (a) Zeng, C. J.; Chen, Y. X.; Kirschbaum, K.; Lambright, K. J.; Jin, R. C. Emergence of Hierarchical Structural Complexities in Nanoparticles and Their Assembly. *Science* **2016**, *354*, 1580-1584; (b) Tian, S. B.; Li, Y. Z.; Li, M. B.; Yuan, J. Y.; Yang, J. L.; Wu, Z. K.; Jin, R. C. Structural Isomerism in Gold Nanoparticles Revealed by X-Ray Crystallography. *Nat Commun* **2015**, *6*, 10012; (c) Liu, C.; Li, T.; Abroshan, H.; Li, Z. M.; Zhang, C.; Kim, H. J.; Li, G.; Jin, R. C. Chiral Ag_{23} Nanocluster with Open Shell Electronic Structure and Helical Face-Centered Cubic Framework. *Nat Commun* **2018**, *9*, 744; (d) Jin, R. C.; Zeng, C. J.; Zhou, M.; Chen, Y. X. Atomically Precise Colloidal Metal Nanoclusters and Nanoparticles: Fundamentals and Opportunities. *Chem. Rev.* **2016**, *116*, 10346-10413; (e) Zeng, C. J.; Liu, C.; Chen, Y. X.; Rosi, N. L.; Jin, R. C. Atomic Structure of Self-Assembled Monolayer of Thiolates on a Tetragonal Au_{92} Nanocrystal. *J. Am. Chem. Soc.* **2016**, *138*, 8710-8713; (f) Higaki, T.; Liu, C.; Zhou, M.; Luo, T. Y.; Rosi, N. L.; Jin, R. C. Tailoring the Structure of 58-Electron Gold Nanoclusters: $Au_{103}S_2(S\text{-}Nap)_{41}$ and Its Implications. *J. Am. Chem. Soc.* **2017**, *139*, 9994-10001; (g) Li, J.; Li, X.; Zhai, H. J.; Wang, L. S. Au_{20}: A Tetrahedral Cluster. *Science* **2003**, *299*, 864; (h) Lei, Z.; Li, J. J.; Wan, X. K.; Zhang, W. H.; Wang, Q. M. Isolation and Total Structure Determination of an All‐Alkynyl‐Protected Gold Nanocluster Au_{144}. *Angew. Chem., Int. Ed.* **2018**, *8639-8643*; (i) Wan, X. K.; Wang, J. Q.; Nan, Z. A.; Wang, Q. M. Ligand Effects in Catalysis by Atomically Precise Gold Nanoclusters. *Sci. Adv.* **2017**, *3* e1701823; (j) Wan, X. K.; Guan, Z. J.; Wang, Q. M. Homoleptic Alkynyl-Protected Gold Nanoclusters: $Au_{44}(PhC{\equiv}C)_{28}$ and $Au_{36}(PhC{\equiv}C)_{24}$. *Angew. Chem., Int. Ed.* **2017**, *56*, 11494-11497; (k) Wan, X. K.; Cheng, X. L.; Tang, Q.; Han, Y. Z.; Hu, G. X.; Jiang, D.; Wang, Q. M. Atomically Precise Bimetallic $Au_{19}Cu_{30}$ Nanocluster with an Icosidodecahedral Cu_{30} Shell and an Alkynyl-Cu Interface. *J. Am. Chem. Soc.* **2017**, *139*, 9451-9454.

4) (a) Zeng, J. L.; Guan, Z. J.; Du, Y.; Nan, Z. A.; Lin, Y. M.; Wang, Q. M. Chloride-Promoted Formation of a Bimetallic Nanocluster $Au_{80}Ag_{30}$ and the Total Structure Determination. *J. Am. Chem. Soc.* **2016**, *138*, 7848-7851; (b) Wang, Y.; Wan, X. K.; Ren, L.; Su, H.; Li, G.; Malola, S.; Lin, S.; Tang, Z.; Häkkinen, H.; Teo, B. K.; Wang, Q. M.; Zheng, N. Atomically Precise Alkynyl-Protected Metal Nanoclusters as a Model Catalyst: Observation of Promoting Effect of Surface Ligands on Catalysis by Metal Nanoparticles. *J. Am. Chem. Soc.* **2016**, *138*, 3278-3281; (c) Wang, Z. Y.; Wang, M. Q.; Li, Y. L.; Luo, P.; Jia, T. T.; Huang, R. W.; Zang, S. Q.; Mak, T. C. W. Atomically Precise Site-Specific Tailoring and Directional Assembly of Superatomic Silver Nanoclusters. *J. Am. Chem. Soc.* **2018**, *140*, 1069-1076; (d) Li, S.; Du, X. S.; Li, B.; Wang, J. Y.; Li, G. P.; Gao, G. G.; Zang, S. Q. Atom-Precise Modification of Silver(I) Thiolate Cluster by Shell Ligand Substitution: A New Approach to Generation of Cluster Functionality and Chirality. *J. Am. Chem. Soc.* **2018**, *140*, 594-597; (e) Yao, Q. F.; Yuan, X.; Fung, V.; Yu, Y.; Leong, D. T.; Jiang, D. E.; Xie, J. P. Understanding Seed-Mediated Growth of Gold Nanoclusters at Molecular Level. *Nat. Commun.* **2017**, *8*, 927; (f) Chen, T.; Yao, Q.; Nasaruddin, R. R.; Xie, J. Electrospray Ionization Mass Spectrometry: A Powerful Platform for Noble-Metal Nanocluster Analysis. *Angew. Chem., Int. Ed.* **2019**, *58*, 11967-11977.

5) (a) Moret, M. E.; Zhang, L.; Peters, J. C. A Polar Copper-Boron One-Electron σ-Bond. *J. Am. Chem. Soc.* **2013**, *135*, 3792-3795; (b)

Weinberger, D. S.; Amin Sk, N.; Mondal, K. C.; Melaimi, M.; Bertrand, G.; Stückl, A. C.; Roesky, H. W.; Dittrich, B.; Demeshko, S.; Schwederski, B.; Kaim, W.; Jerabek, P.; Frenking, G. Isolation of Neutral Mononuclear Copper Complexes Stabilized by Two Cyclic (Alkyl)(amino)carbenes. *J. Am. Chem. Soc.* **2014**, *136*, 6235-6238.

6) Dhayal, R. S.; Liao, J. H.; Lin, Y. R.; Liao, P. K.; Kahlal, S.; Saillard, J. Y.; Liu, C. W. A Nanospheric Polyhydrido Copper Cluster of Elongated Triangular Orthobicupola Array: Liberation of H_2 from Solar Energy. *J. Am. Chem. Soc.* **2013**, *135*, 4704-4707.

7) Edwards, A. J.; Dhayal, R. S.; Liao, P. K.; Liao, J. H.; Chiang, M. H.; Piltz, R. O.; Kahlal, S.; Saillard, J. Y.; Liu, C. W. Chinese Puzzle Molecule: A 15 Hydride, 28 Copper Atom Nanoball. *Angew. Chem., Int. Ed.* **2014,** *53*, 7214-7218.

8) Dhayal, R. S.; Liao, J. H.; Kahlal, S.; Wang, X.; Liu, Y. C.; Chiang, M. H.; van Zyl, W. E.; Saillard, J. Y.; Liu, C. W. $[Cu_{32}(H)_{20}\{S_2P(O^iPr)_2\}_{12}]$: The Largest Number of Hydrides Recorded in a Molecular Nanocluster by Neutron Diffraction. *Chem. -Eur. J.* **2015,** *21*, 8369-8374.

9) Ganesamoorthy, C.; Weßing, J.; Kroll, C.; Seidel, R. W.; Gemel, C.; Fischer, R. A. The Intermetalloid Cluster $[(Cp^*AlCu)_6H_4]$, Embedding a Cu_6 Core Inside an Octahedral Al_6 Shell: Molecular Models of Hume-Rothery Nanophases. *Angew. Chem., Inter. Ed.* **2014,** *53*, 7943-7947.

10) Nguyen, T. A. D.; Jones, Z. R.; Goldsmith, B. R.; Buratto, W. R.; Wu, G.; Scott, S. L.; Hayton, T. W. A Cu_{25} Nanocluster with Partial Cu(0) Character. *J. Am. Chem. Soc.* **2015,** *137*, 13319-13324.

11) Nguyen, T. A. D.; Jones, Z. R.; Leto, D. F.; Wu, G.; Scott, S. L.; Hayton, T. W. Ligand-Exchange-Induced Growth of an Atomically Precise Cu_{29} Nanocluster from a Smaller Cluster. *Chem. Mater.* **2016,** *28*, 8385-8390.

12) Weßing, J.; Ganesamoorthy, C.; Kahlal, S.; Marchal, R.; Gemel, C.; Cador, O.; Da Silva, A. C. H.; Da Silva, J. L. F.; Saillard, J. Y.; Fischer, R. A. The Mackay-Type Cluster $[Cu_{43}Al_{12}](Cp^*)_{12}$: Open-Shell 67-Electron Superatom with Emerging Metal-Like Electronic Structure. *Angew. Chem., Int. Ed.* **2018,** *57*, 14630-14634.

13) Chakrahari, K. K.; Liao, J. H.; Kahlal, S.; Liu, Y. C.; Chiang, M. H.; Saillard, J. Y.; Liu, C. W. $[Cu_{13}\{S_2CN^nBu_2\}_6(acetylide)_4]^+$: A Two-Electron Superatom. *Angew. Chem., Int. Ed.* **2016,** *55*, 14704-14708.

14) Yuan, P.; Chen, R.; Zhang, X.; Chen, F.; Yan, J.; Sun, C.; Ou, D.; Peng, J.; Lin, S.; Tang, Z.; Teo, B. K.; Zheng, L. S.; Zheng, N. Ether-Soluble Cu_{53} Nanoclusters as an Effective Precursor of High-Quality CuI Films for Optoelectronic Applications. *Angew. Chem., Inter. Ed.* **2019,** *58*, 835-839.

15) Zhang, L. M.; Mak, T. C. W. Comproportionation Synthesis of Copper(I) Alkynyl Complexes Encapsulating Polyoxomolybdate Templates: Bowl-Shaped Cu_{33} and Peanut-Shaped Cu_{62} Nanoclusters. *J. Am. Chem. Soc.* **2016,** *138*, 2909-2912.

16) Zhuo, H. Y.; Su, H. F.; Cao, Z. Z.; Liu, W.; Wang, S. A.; Feng, L.; Zhuang, G. L.; Lin, S. C.; Kurmoo, M.; Tung, C. H.; Sun, D.; Zheng, L. S. High-Nuclear Organometallic Copper(I)-Alkynide Clusters: Thermochromic Near-Infrared Luminescence and Solution Stability. *Chem. -Eur. J.* **2016,** *22*, 17619-17626.

17) (a) Qiao, J.; Shi, K.; Wang, Q.-M., A Giant Silver Alkynyl Cage with Sixty Silver(I) Ions Clustered around Polyoxometalate Templates. *Angew. Chem., Int. Ed.* **2010,** *49*, 1765-1767. (b) Li, G.; Lei, Z.; Wang, Q.-M., Luminescent Molecular Ag-S Nanocluster $[Ag_{62}S_{13}(SBu^t)_{32}](BF_4)_4$. *J. Am. Chem. Soc.* **2010,** *132*, 17678-17679. (c) Wilson, E. F.; Abbas, H.; Duncombe, B. J.; Streb, C.; Long, D. L.; Cronin, L., Probing the Self-assembly of Inorganic Cluster Architectures in Solution with Cryospray Mass Spectrometry: Growth of Polyoxomolybdate Clusters and Polymers Mediated by Silver(I) ions. *J. Am. Chem. Soc.* **2008,** *130*, 13876-13884.

18) Spek, A. L. Structure Validation in Chemical Crystallography. *Acta Crystallogr., Sect. D: Biol. Crystallogr.* **2009,** *65*, 148-155.

19) Li, Y. L.; Wang, J.; Luo, P.; Ma, X. H.; Dong, X. Y.; Wang, Z. Y.; Du, C. X.; Zang, S. Q.; Mak, T. C. W., Cu_{14} Cluster with Partial Cu(0) Character: Difference in Electronic Structure from Isostructural Silver Analog. *Adv. Sci.* **2019**, 1900833.

20) Qian, H. F.; Eckenhoff, W. T.; Zhu, Y.; Pintauer, T.; Jin, R. C., Total Structure Determination of Thiolate-Protected Au_{38} Nanoparticles. *J. Am. Chem. Soc.* **2010,** *132*, 8280-8281.

21) Wyckoff, R. W. G. *Crystal Structures*, 2nd ed.; Interscience Publishers: New York, 1963; Vol. *1*.

22) Kang, X.; Zhu, M. Intra-cluster Growth Meets Inter-cluster Assembly: The Molecular and Supramolecular Chemistry of Atomically Precise Nanoclusters. *Coord. Chem. Rev.* **2019,** *394*, 1-38.

23) Cook, A. W.; Jones, Z. R.; Wu, G.; Scott, S. L.; Hayton, T. W. An Organometallic Cu_{20} Nanocluster: Synthesis, Characterization, Immobilization on Silica, and "Click" Chemistry. *J. Am. Chem. Soc.* **2018,** *140*, 394-400.

24) (a) Das, A.; Li, T.; Nobusada, K.; Zeng, C. J.; Rosi, N. L.; Jin, R. C., Nonsuperatomic $[Au_{23}(SC_6H_{11})_{16}]^-$ Nanocluster Featuring Bipyramidal Au_{15} Kernel and trimeric $Au_3(SR)_4$ Motif. *J. Am. Chem. Soc.* **2013,** *135*, 18264-18267. (b) Wan, X.-K.; Yuan, S.-F.; Tang, Q.; Jiang, D.-e.; Wang, Q.-M., Alkynyl-Protected Au_{23} Nanocluster: A 12-Electron System. *Angew Chem Int Ed* **2015,** *54*, 5977-5980.

25) (a) Hakkinen, H., Atomic and Electronic Structure of Gold Clusters: Understanding Flakes, Cages and Superatoms from Simple Concepts. *Chem. Soc. Rev.* **2008,** *37*, 1847-1859. (b) Walter, M.; Akola, J.; Lopez-Acevedo, O.; Jadzinsky, P. D.; Calero, G.; Ackerson, C. J.; Whetten, R. L.; Groenbeck, H.; Hakkinen, H., A Unified View of Ligand-Protected Gold Clusters as Superatom Complexes. *Proc Natl Acad Sci USA* **2008,** *105*, 9157-9162.

Table of Content